




Transient chiral dynamics revealed by two-dimensional circular dichroism spectroscopyZihui Liu ¹, Ajay Jha ^{2,3,4}, Xian-Ting Liang,^{1,*} and Hong-Guang Duan ^{1,†}¹*Department of Physics, School of Physical Science and Technology, Ningbo University, Ningbo 315211, P.R. China*²*Rosalind Franklin Institute, Harwell, Oxfordshire OX11 0QX, United Kingdom*³*Department of Pharmacology, University of Oxford, Oxford OX1 3QT, United Kingdom*⁴*Research Complex at Harwell, Rutherford Appleton Laboratory, Didcot OX11 0QX, United Kingdom*

(Received 25 September 2022; revised 21 February 2023; accepted 5 May 2023; published 18 May 2023)

Chirality has been considered as one of the key factors in the evolution of life in nature. It is important to uncover how chiral potentials of molecular systems play vital role in fundamental photochemical processes. Here, we investigate the role of chirality in photoinduced energy transfer in a model dimeric system, where the monomers are excitonically coupled. To observe transient chiral dynamics and energy transfer, we employ circularly polarized laser pulses in two-dimensional electronic spectroscopy to construct the two-dimensional circular dichroism (2DCD) spectral maps. Tracking time-resolved peak magnitudes in 2DCD spectra allows one to identify chirality induced population dynamics. The dynamics of energy transfer is revealed by the time-resolved kinetics of cross peaks. However, the differential signal of 2DCD spectra shows the magnitude of cross peaks is dramatically reduced at initial waiting time, which indicates the weak chiral interactions between two monomers. The downhill energy transfer is resolved by presenting a strong magnitude of cross peak in 2DCD spectra after long waiting time. The chiral contribution towards coherent and incoherent energy-transfer pathways in the model dimer system is further examined via control of excitonic couplings between two monomers. Applications are made to study the energy-transfer process in the Fenna-Matthews-Olson complex. Our work uncovers the potential of 2DCD spectroscopy to resolve the chiral-induced interactions and population transfers in excitonically coupled systems.

DOI: [10.1103/PhysRevE.107.054119](https://doi.org/10.1103/PhysRevE.107.054119)**I. INTRODUCTION**

Chirality is a fundamental feature of biological life. It refers to chemically identical molecular species having nonsuperimposable structural arrangements [1]. Steady-state circular dichroism (CD) is a standard analytical tool for measuring chirality in chemistry and biology, where CD denotes the difference in absorption of left- and right-handed circularly polarized light in chiral molecular systems. In the deep UV, the CD absorption is quite useful to examine the protein structure by interacting to the transition dipoles of amino acids and nucleotides [2]. Consequently, time-resolved CD spectroscopy has been considered as a promising experimental tool that is sensitive to the changes of biomolecular configuration as a function of time, combining the information of electronic transitions from traditional transient absorption spectroscopy. Recently, Oppermann *et al.* developed an ultrafast CD spectrometer with broadband pulses in deep UV range [3]. The excellent signal-to-noise ratio (10^{-5} OD) allows us to track the weak chiral dynamics of Ru-complex during the process of metal-to-ligand charge transfer. The earlier work of transient absorption with chiral light has been performed two decades ago [4]. The pump-probe spectroscopy provides the information of underlying energy and population transfers,

but the coherent dynamics associated with the process cannot be revealed. The two-dimensional electronic spectroscopy (2DES) is a valuable tool to examine the quantum coherence during the process of energy transfers [5–9]. The phase-locked techniques and the heterodyne detection allows 2DES to detect the quantum electronic and vibrational coherences with a decent signal-to-noise ratio (SNR). Recently, it has been extensively employed to study the energy transfers in photosynthetic protein complexes [10–13], solid-state materials [14,15], and molecules in the gas phase [16]. The chiral dynamics of photosynthetic protein complex (LH2) has been studied by 2DES with polarization dependent measurement [17]. After the careful selection of the polarization of each laser pulse, the 2DES is able to suppress the achiral signal from the chiral contribution. However, the circularly polarized light has not been employed to study its interaction with magnetic dipole and quadruple moments, which is fundamental to the chiral interaction between light and matter.

Theoretically, the transient chiral dynamics has been calculated by *ab initio* methods at different wavelength. Cho *et al.* have proposed to calculate the circularly polarized transient absorption spectra by response-function theory [18] and the calculations have been extended to the IR region for the study of basic elements in protein structure [19]. Mukamel *et al.* calculated the 2DES in ultraviolet region of the spectrum to study the structural dynamics of protein backbone [20]. The perpendicular configuration of linearly polarized field of the first two pulses are employed to separate the

*liangxianting@nbu.edu.cn

†duanhongguang@nbu.edu.cn

transient chiral signals from achiral part. The resonant x-ray spectroscopy has been employed to explore the photoinduced molecular chirality [21]. The time-resolved circular dichroism signals are calculated by difference of left and right circularly polarized x-ray probe transmission following an excitation by a circularly polarized optical pump with the variable time delay. Recently, the chiral four-wave-mixing signals are also calculated with circularly polarized x-ray pulses, which has been used to analyze chiral stimulated x-ray Raman signals at the carbon *K*-edge and chiral visible 2DES of the valence excitations of S-ibuprofen [22]. The utilization of circularly polarized laser pulses in 2DES to investigate coherence in energy-transfer processes and, especially, the interactions of magnetic-dipole or -quadruple moments with matter have not yet been fully investigated despite these rigorous investigations in many wavelength areas. Additionally, the time-resolved chiral dynamics of 2DES and its detailed relation to the chiral molecular structure is still elusive.

In this paper, we employ the circularly polarized laser pulses in 2DES and study the transient chiral dynamics of energy transfer in an excitonically coupled dimer system. For this, the electronic and magnetic-dipole moments have been used to construct the response function for the calculation of 2DES. We tune the strength of electronic coupling between two monomers to examine the coherent and incoherent population transfers and its relation to the molecular chiral structure. The 2DCD data show two diagonal peaks with positive and negative amplitudes corresponding to the spectral features of steady-state CD spectrum. The coherent and incoherent contributions to chirality induced energy transfer have been examined in different excitonic coupling strength regimes. Additionally, the electronic quantum coherence is also observed in the 2DCD spectral dynamics during the process of energy transfer. Our work provides careful comparison between 2DCD and 2DES spectra to show that the 2DCD provide a rich spectroscopic signal.

II. THEORETICAL MODEL

A. Hamiltonian

We employ the system-bath model to calculate the linear absorption and 2DES. The model Hamiltonian can be written as

$$H = H_S + H_B + H_{SB}, \quad (1)$$

where H_S indicates the system Hamiltonian and is given as

$$H_S = \sum_{m=1}^N \epsilon_m |m\rangle \langle m| + \sum_{m=1}^N \sum_{n < m} J_{n,m} |m\rangle \langle n| + |n\rangle \langle m|, \quad (2)$$

ϵ_m and $J_{n,m}$ is the m th site energy and the excitonic coupling between n th and m th pigments, respectively. N is the total number of pigments; for a dimer, $N = 2$. The bath Hamiltonian can be written as

$$H_B = \sum_{m=1}^N \sum_{j=1}^{N_b^m} \left(\frac{p_{mj}^2}{2} + \frac{1}{2} \omega_{mj} x_{mj}^2 \right), \quad (3)$$

where N_b^m is the total number of bath modes coupled to the m th molecule. x_{mj} and p_{mj} are the mass-weighted position

and momentum of j th harmonic-oscillator bath mode with frequency ω_{mj} . The interaction term $H_{SB} = \sum_m K_m \Phi_m(x)$ describes the coupling between system and bath. It is assumed to be separable such that K_m only acts on system subspace and $\Phi_m(x)$ only on the bath degrees of freedom. In the following, we further assume a linear relation between bath coordinates and the system. The system-bath interaction is then given as

$$H_{SB} = \sum_m K_m \sum_j c_{mj} x_{mj}. \quad (4)$$

The influence of the bath is fully described by its bath spectral density

$$J_m(\omega) = \pi \sum_j \frac{c_{mj}}{2m_{mj}\omega_{mj}} \delta(\omega - \omega_{mj}) = 2\lambda \frac{\omega\gamma}{\omega^2 + \gamma^2}. \quad (5)$$

Here, we take the Lorentzian type of spectral density with Drude cutoff frequency, which has been used in related studies [23–25]. λ and γ are the reorganization energy and high-frequency cutoff. We assume the identical spectral densities of all the baths, i.e., $J_n(\omega) = J_m(\omega)$.

The laser pulse interacting with molecules can be described by the interaction Hamiltonian H_{int} , which is given as

$$H_{\text{int}} = -\boldsymbol{\mu} \cdot \mathbf{E}(t) - \mathbf{m} \cdot \mathbf{B}(t) - \mathbf{q} \cdot \nabla \mathbf{E}(t), \quad (6)$$

where $\boldsymbol{\mu}$ is the transition electric-dipole moment, \mathbf{m} is the transition magnetic-dipole moment, and \mathbf{q} is quadrupole. $\mathbf{E}(t)$ and $\mathbf{B}(t)$ are the electric and magnetic fields, respectively. For each electric and magnetic field, one has

$$\begin{aligned} \mathbf{E}(t) &= E_0 f(t) e^{i\mathbf{k}\cdot\mathbf{r} - i\omega t} \mathbf{e} + \text{c.c.}, \\ \mathbf{B}(t) &= B_0 f(t) e^{i\mathbf{k}\cdot\mathbf{r} - i\omega t} \mathbf{b} + \text{c.c.}, \end{aligned} \quad (7)$$

where E_0 and B_0 are the related amplitudes and $f(t)$ is the pulse envelope function. The vectors of electric and magnetic-field polarization directions are \mathbf{e} and \mathbf{b} , respectively. We assume the left- and right-circularly polarized waves propagating along the z direction \mathbf{e}_z . The vector \mathbf{b} , is orthogonal to both \mathbf{e}_z and \mathbf{e}_L and \mathbf{e}_R as [26]

$$\mathbf{b}_L = \frac{1}{c} \mathbf{e}_z \times \mathbf{e}_L, \quad \mathbf{b}_R = \frac{1}{c} \mathbf{e}_z \times \mathbf{e}_R. \quad (8)$$

The left- and right-circularly polarized waves have polarization vectors [18]

$$\mathbf{e}_L = \frac{1}{\sqrt{2}} (\mathbf{e}_x + i\mathbf{e}_y), \quad \mathbf{e}_R = -\frac{1}{\sqrt{2}} (\mathbf{e}_x - i\mathbf{e}_y). \quad (9)$$

Furthermore, the magnetic-field polarization directions

$$\mathbf{b}_L = -i\mathbf{e}_L, \quad \mathbf{b}_R = i\mathbf{e}_R. \quad (10)$$

For the CD in the linear regime, the contribution of the electric-quadrupole moment vanishes due to the rotational averaging factors. For the nonlinear chirality-induced signals, the importance of magnetic field and electric quadrupole electric field cannot be neglected [27,28]. However, due to the rotational averaging factors, the overall quadrupole contribution is an order of magnitude smaller than the magnetic-dipole contribution [29]. In Refs. [18,30], the researchers eliminated the contribution of quadrupole-electric field gradient interactions by controlling the beam propagation direction. For

simplicity, we ignore the signal from quadrupole moment in this work.

B. Theoretical description of chirality-induced signals

CD denotes the difference in absorption between left- and right-polarized light,

$$\Delta\varepsilon = \varepsilon_L - \varepsilon_R. \quad (11)$$

The differential absorbance $\Delta\varepsilon$ is plotted against the wavelength λ to yield the CD spectrum. The integral of $\Delta\varepsilon$ over a wavelength range associated with a particular transition is known as the CD strength or rotational strength of that transition. From the quantum electrodynamic viewpoint, the rotational strength [31] R_{0n} of a transition from the ground state 0 to an electronically excited state n is the product of the electric transition dipole moment and the magnetic transition dipole moment:

$$R_{0n} = \text{Im}(\boldsymbol{\mu}_{0n} \cdot \mathbf{m}_{n0}). \quad (12)$$

$\boldsymbol{\mu}$ describes a linear displacement, whereas \mathbf{m} characterizes a circulation of charge [2]. Thus, the combination of $\boldsymbol{\mu}$ and \mathbf{m} creates a helical displacement of charge, leading to a different interaction with left- and right-circularly polarized light. While the operator for $\boldsymbol{\mu}$ is a real vector, that for \mathbf{m} is imaginary because it describes the rotation of charge in a complex coordinate system [32] and it is origin-dependent [33]:

$$\mathbf{m} = \frac{e}{2mc} \mathbf{r} \times \mathbf{p}, \quad \mathbf{p} = \frac{\hbar}{i} \nabla, \quad (13)$$

where e is the charge, m the mass of the electron, c the speed of light, where \mathbf{r} is the position operator of the electron, \mathbf{p} is the linear momentum of the monomer, and ∇ is the gradient operator. For the study of a specific system, the electric and magnetic transition dipoles can be calculated by quantum chemistry methods [22,29].

We use time-dependent perturbation theory [34] with the treatment of H_{int} to calculate the optical spectroscopy. The quantum Liouville equation is given as

$$\begin{aligned} \frac{\partial \rho(t)}{\partial t} &= -\frac{i}{\hbar} [H - H_{\text{int}}, \rho(t)] - \frac{i}{\hbar} [H_{\text{int}}, \rho(t)] \\ &= -\frac{i}{\hbar} O^\times \rho(t) - \frac{i}{\hbar} O_I^\times \rho(t). \end{aligned} \quad (14)$$

The formal expression of the first-order and the third-order polarization are given as

$$\begin{aligned} \mathbf{P}^{(1)}(t) &= \int_0^\infty dt_1 F(t-t_1) R^{(1)}(t_1), \\ \mathbf{P}^{(3)}(t) &= \int_0^\infty dt_3 \int_0^\infty dt_2 \int_0^\infty dt_1 F_3(t-t_3) \\ &\quad \times F_2(t-t_3-t_2) F_1(t-t_3-t_2-t_1) R^{(3)}(t_3, t_2, t_1), \end{aligned} \quad (15)$$

with

$$\begin{aligned} R^{(1)}(t_1) &\propto i \langle O_I G(t_1) O_I^\times \rho(-\infty) \rangle, \\ R^{(3)}(t_3, t_2, t_1) &\propto -i \langle O_I G(t_3) O_I^\times G(t_2) O_I^\times G(t_1) O_I^\times \rho(-\infty) \rangle, \end{aligned} \quad (16)$$

where $F(t)$ is the external field and O_I is the conjugate operator that induces quantum transitions between any two different quantum states. For any operator O , it shows $O^\times \rho = [O, \rho]$ and the time evolution operators $G(t)\rho = e^{-iH_S t} \rho e^{iH_S t}$. In this paper, we employ the Redfield quantum master equation [35] to calculate the time-evolved dynamics.

We insert $H_{\text{int}} = -\boldsymbol{\mu} \cdot \mathbf{E}(t) - \mathbf{m} \cdot \mathbf{B}(t) - \mathbf{q} \cdot \nabla \mathbf{E}(t)$ into Eq. (14), we find $\mathbf{P}^{(3)}$ can be expanded as

$$\mathbf{P}^{(3)}(t) = \mathbf{P}_0^{(3)}(t) + \delta \mathbf{P}^{(3)}(t, \mathbf{m}) + \delta \mathbf{P}^{(3)}(t, \mathbf{q}) + \dots \quad (17)$$

The first term on the right-hand side involves only the electric-dipole transitions and it is dominant in the signal of the third-order polarization. The second and third terms are linearly proportional to the magnetic-dipole and electric-quadrupole moments, respectively. The optical activity signal can be defined as the difference between two signals obtained with the left- and right-circularly polarized beams as [18,22,29]

$$\Delta S = S(L) - S(R). \quad (18)$$

Here, the subscripts L and R represent the cases when the polarization property of the injected beam is left- and right-circularly polarized, respectively.

The first terms in Eq. (17) are identical regardless of the rotation direction of the injected circularly polarized pulse, it cannot provide information on the optical activity of chiral molecules in solution. In contrast, the second and third terms depend on the molecular chirality and the rotational direction of the injected circularly polarized beam. Thus, we name this part of signal as chirality-induced signals.

C. Linear response

The steady-state CD spectrum is calculated from the first-order signal, which usually contains the chiral and achiral contributions,

$$S_{\text{het}}^{(1)}(\Gamma) = S_{\text{achir}}^{(1)}(\Gamma) + S_{\text{chir}}^{(1)}(\Gamma), \quad (19)$$

where Γ contains the set of parameters that control the signal (field-matter interaction times, laser pulses polarizations, wave vector configuration, central frequencies, bandwidths). The achiral part is purely given by electric-dipole moment,

$$S_{\text{achir}}^{(1)}(\Gamma) = \int dt dt_1 R_{\mu\mu}^{(1)}(t_1) \cdot [\mathbf{E}_S(t) \otimes \mathbf{E}_1(t-t_1)], \quad (20)$$

with

$$R_{\mu\mu}^{(1)}(t_1) = i \langle \boldsymbol{\mu} G(t_1) \boldsymbol{\mu}^\times \rho(-\infty) \rangle. \quad (21)$$

The chiral part is contributed by multipolar interaction,

$$\begin{aligned} S_{\text{chir}}^{(1)}(\Gamma) &= \int dt dt_1 \{ R_{m\mu}^{(1)}(t_1) \cdot [\mathbf{B}_S(t) \otimes \mathbf{E}_1(t-t_1)] \\ &\quad + R_{\mu m}^{(1)}(t_1) \cdot [\mathbf{E}_S(t) \otimes \mathbf{B}_1(t-t_1)] \\ &\quad + R_{qm}^{(1)}(t_1) \cdot [\nabla \mathbf{E}_S(t) \otimes \mathbf{E}_1(t-t_1)] \\ &\quad + R_{\mu q}^{(1)}(t_1) \cdot [\mathbf{E}_S(t) \otimes \nabla \mathbf{E}_1(t-t_1)] \}, \end{aligned} \quad (22)$$

with

$$R_{m\mu}^{(1)}(t_1) = i \langle \mathbf{m} G(t_1) \boldsymbol{\mu}^\times \rho(-\infty) \rangle, \quad (23)$$

and

$$R_{q\mu}^{(1)}(t_1) = i\langle qG(t_1)\boldsymbol{\mu}^\times \rho(-\infty) \rangle, \quad (24)$$

respectively. \mathbf{E}_1 and \mathbf{B}_1 denote the electric and magnetic fields of incoming beams. \mathbf{E}_S and \mathbf{B}_S denote the electric and magnetic fields of probe beams. $G(t)$ indicates the time-evolution operator. $\rho(-\infty)$ is a density operator at the negative infinity time. For the electric-dipole moment operator, we show $\mu = \mu_+ + \mu_-$ with $\mu_+ = \sum_{n=1}^N \mu_n |n\rangle \langle 0|$ and $\mu_- = \sum_{n=1}^N \mu_n |0\rangle \langle n|$. For the magnetic-dipole moment, it shows $m = m_+ + m_-$, where $m_+ = \sum_{n=1}^N iM_n |n\rangle \langle 0|$ and $m_- = \sum_{n=1}^N -iM_n |0\rangle \langle n|$. μ_n and M_n are real values.

We employ the delta-pulse approximation to simplify the expression. By this, we can move the electric field outside of the integral. Then, the Eqs. (20) and (22) can be simplified as follows:

$$S_{\text{achir}}^{(1)}(\Gamma) = R_{\mu\mu}^{(1)}(t_1) \cdot (\mathbf{E}_S \otimes \mathbf{E}_1), \quad (25)$$

and

$$S_{\text{chir}}^{(1)}(\Gamma) = [R_{m\mu}^{(1)}(t_1) \cdot (\mathbf{B}_S \otimes \mathbf{E}_1) + R_{\mu m}^{(1)}(t_1) \cdot (\mathbf{E}_S \otimes \mathbf{B}_1) + R_{q\mu}^{(1)}(t_1) \cdot (\nabla \mathbf{E}_S \otimes \mathbf{E}_1) + R_{\mu q}^{(1)}(t_1) \cdot (\mathbf{E}_S \otimes \nabla \mathbf{E}_1)], \quad (26)$$

respectively. The linear absorption spectrum $S_{\text{het}}^{(1)}(\Gamma, \Omega)$ is obtained by Fourier transform of $S_{\text{het}}^{(1)}(\Gamma)$ over t_1 . The CD spectrum can be written as the signal difference between left- and right-circularly polarized light,

$$CD(\omega) = S_{\text{het}}^{(1)}(L, L, \Omega) - S_{\text{het}}^{(1)}(R, R, \Omega), \quad (27)$$

where (L, L) and (R, R) denote the fields interacting with matter by left and right polarization. It is noticeable that, in Eq. (27), the nonchiral contribution is canceled and the contribution of the electric-quadrupole moment to the CD spectrum also disappear due to the rotational average.

D. Nonlinear response

We consider the four-wave-mixing signal, which is denoted as \mathbf{k}_I and \mathbf{k}_{II} according to the phase matching directions

$$\mathbf{k}_I = -\mathbf{k}_1 + \mathbf{k}_2 + \mathbf{k}_3, \quad \mathbf{k}_{II} = +\mathbf{k}_1 - \mathbf{k}_2 + \mathbf{k}_3, \quad (28)$$

where \mathbf{k}_1 , \mathbf{k}_2 , and \mathbf{k}_3 are the wave vectors of the time-ordered incoming pulses. The third-order signal of \mathbf{k}_I and \mathbf{k}_{II} contains three contributions, ground-state bleaching (GSB), stimulated emission (SE), and excited-state absorption (ESA), respectively.

Consequently, the third-order $S_{\text{het}}^{(3)}(\Gamma)$ contains the chiral and achiral contributions, it can be described as

$$S_{\text{het}}^{(3)}(\Gamma) = S_{\text{achir}}^{(3)}(\Gamma) + S_{\text{chir}}^{(3)}(\Gamma), \quad (29)$$

and

$$S_{\text{achir}}^{(3)}(\Gamma) = \int dt dt_3 dt_2 dt_1 R_{\mu\mu\mu\mu}^{(3)}(t_3, t_2, t_1) \cdot [\mathbf{E}_S(t) \otimes \mathbf{E}_3(t-t_3) \otimes \mathbf{E}_2(t-t_3-t_2) \otimes \mathbf{E}_1(t-t_3-t_2-t_1)], \quad (30)$$

with

$$R_{\mu\mu\mu\mu}^{(3)}(t_3, t_2, t_1) = -i\langle \boldsymbol{\mu}G(t_3)\boldsymbol{\mu}^\times G(t_2)\boldsymbol{\mu}^\times G(t_1)\boldsymbol{\mu}^\times \rho(-\infty) \rangle. \quad (31)$$

In Eq. (31), $R_{\mu\mu\mu\mu}^{(3)}(t_3, t_2, t_1)$ is a sum of pathways with four electric dipoles. At the lowest multipolar order, the chiral contribution $S_{\text{chir}}^{(3)}$ contains either one magnetic dipole or one electric quadrupole, which is given by Ref. [22]. Then it shows

$$S_{\text{chir}}^{(3)}(\Gamma) = \int dt dt_3 dt_2 dt_1 [R_{m\mu\mu\mu}^{(3)} \cdot (\mathbf{B}_S \otimes \mathbf{E}_3 \otimes \mathbf{E}_2 \otimes \mathbf{E}_1) + R_{q\mu\mu\mu}^{(3)} \cdot (\nabla \mathbf{E}_S \otimes \mathbf{E}_3 \otimes \mathbf{E}_2 \otimes \mathbf{E}_1) + R_{\mu m\mu\mu}^{(3)} \cdot (\mathbf{E}_S \otimes \mathbf{B}_3 \otimes \mathbf{E}_2 \otimes \mathbf{E}_1) + R_{\mu q\mu\mu}^{(3)} \cdot (\mathbf{E}_S \otimes \nabla \mathbf{E}_3 \otimes \mathbf{E}_2 \otimes \mathbf{E}_1) + R_{\mu\mu m\mu}^{(3)} \cdot (\mathbf{E}_S \otimes \mathbf{E}_3 \otimes \mathbf{B}_2 \otimes \mathbf{E}_1) + R_{\mu\mu q\mu}^{(3)} \cdot (\mathbf{E}_S \otimes \mathbf{E}_3 \otimes \nabla \mathbf{E}_2 \otimes \mathbf{E}_1) + R_{\mu\mu\mu m}^{(3)} \cdot (\mathbf{E}_S \otimes \mathbf{E}_3 \otimes \mathbf{E}_2 \otimes \mathbf{B}_1) + R_{\mu\mu\mu q}^{(3)} \cdot (\mathbf{E}_S \otimes \mathbf{E}_3 \otimes \mathbf{E}_2 \otimes \nabla \mathbf{E}_1)], \quad (32)$$

with

$$R_{m\mu\mu\mu}^{(3)}(t_3, t_2, t_1) = -i\langle mG(t_3)\boldsymbol{\mu}^\times G(t_2)\boldsymbol{\mu}^\times G(t_1)\boldsymbol{\mu}^\times \rho(-\infty) \rangle, \\ R_{q\mu\mu\mu}^{(3)}(t_3, t_2, t_1) = -i\langle qG(t_3)\boldsymbol{\mu}^\times G(t_2)\boldsymbol{\mu}^\times G(t_1)\boldsymbol{\mu}^\times \rho(-\infty) \rangle. \quad (33)$$

Considering the impulsive limit, we can remove all the integrals in Eqs. (30) and (32), then, we have

$$S_{\text{achir}}^{(3)}(\Gamma) = R_{\mu\mu\mu\mu}^{(3)}(t_3, t_2, t_1) \cdot (\mathbf{E}_S \otimes \mathbf{E}_3 \otimes \mathbf{E}_2 \otimes \mathbf{E}_1), \quad (34)$$

and

$$S_{\text{chir}}^{(3)}(\Gamma) = [R_{m\mu\mu\mu}^{(3)} \cdot (\mathbf{B}_S \otimes \mathbf{E}_3 \otimes \mathbf{E}_2 \otimes \mathbf{E}_1) + R_{q\mu\mu\mu}^{(3)} \cdot (\nabla \mathbf{E}_S \otimes \mathbf{E}_3 \otimes \mathbf{E}_2 \otimes \mathbf{E}_1) + R_{\mu m\mu\mu}^{(3)} \cdot (\mathbf{E}_S \otimes \mathbf{B}_3 \otimes \mathbf{E}_2 \otimes \mathbf{E}_1) + R_{\mu q\mu\mu}^{(3)} \cdot (\mathbf{E}_S \otimes \nabla \mathbf{E}_3 \otimes \mathbf{E}_2 \otimes \mathbf{E}_1) + R_{\mu\mu m\mu}^{(3)} \cdot (\mathbf{E}_S \otimes \mathbf{E}_3 \otimes \mathbf{B}_2 \otimes \mathbf{E}_1) + R_{\mu\mu q\mu}^{(3)} \cdot (\mathbf{E}_S \otimes \mathbf{E}_3 \otimes \nabla \mathbf{E}_2 \otimes \mathbf{E}_1) + R_{\mu\mu\mu m}^{(3)} \cdot (\mathbf{E}_S \otimes \mathbf{E}_3 \otimes \mathbf{E}_2 \otimes \mathbf{B}_1) + R_{\mu\mu\mu q}^{(3)} \cdot (\mathbf{E}_S \otimes \mathbf{E}_3 \otimes \mathbf{E}_2 \otimes \nabla \mathbf{E}_1)]. \quad (35)$$

The 2DES is calculated by Fourier transform of $S_{\text{het}}^{(3)}(\Gamma)$ in Eq. (29) over t_1 and t_3 . The obtained 2DCD spectra is defined as the difference between two nonlinear signals from left- and right-circularly polarized pulses, which shows

$$S_{2\text{DCD}}^{(3)}(\Omega_3, t_2, \Omega_1) = S_{\text{het}}^{(1)}(L, L, L, L, \Omega_3, t_2, \Omega_1) - S_{\text{het}}^{(1)}(R, R, R, R, \Omega_3, t_2, \Omega_1), \quad (36)$$

where (L, L, L, L) and (R, R, R, R) denote the four-time-field-matter interactions with the left or right polarization. The transitions of linear and nonlinear response functions can be described by Feynman diagram, which is presented in Fig. 1.

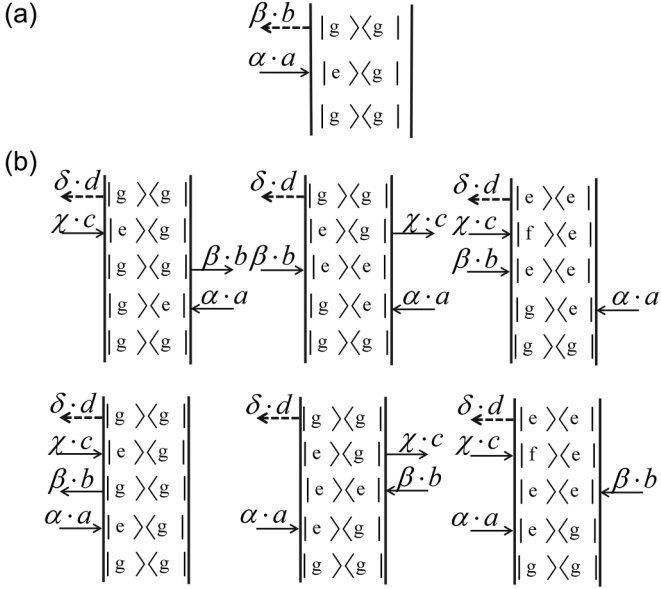


FIG. 1. (a) The Feynman diagrams for first-order linear spectroscopy. (b) The Feynman diagrams for third-order nonlinear spectroscopy. $\alpha \cdot a$, $\beta \cdot b$, $\chi \cdot c$, and $\delta \cdot d$ represent one of $\mu \cdot E$, $m \cdot B$, and $q \cdot \nabla E$. When considering nonchiral signals, we only consider $\mu \cdot E$ interactions. When considering the lowest multipolar order of chiral signals, we need to replace one $\mu \cdot E$ of four by $m \cdot B$ or $q \cdot \nabla E$ and sum up all possible cases.

III. RESULTS AND DISCUSSIONS

First, we assign the parameters in the dimer model. We separate the calculations into two cases: coherent vs incoherent energy transfers. In the case of incoherent energy transfer, we choose $\epsilon_1 = 21459.0 \text{ cm}^{-1}$, $\epsilon_2 = 19011.0 \text{ cm}^{-1}$, and $J_{1,2} = J_{2,1} = 84.6 \text{ cm}^{-1}$ (we took the parameters directly from Ref. [36]). The interaction between two monomers is rather weak compared with the energy gap between them. The parameters of the spectral density are $\lambda = 245.5 \text{ cm}^{-1}$, $\gamma = 2448 \text{ cm}^{-1}$ in Eq. (5). The calculations are performed at room temperature, $T = 300 \text{ K}$. For the simplicity, we assume two transition dipoles are perpendicular to each other, i.e., $\mu_1 = \mu_1 e_x$, with $\mu_1 = 9 \text{ Debye}$, $\mu_2 = \mu_2 e_z$, with $\mu_2 = 5 \text{ Debye}$. The sum rule for rotational strengths [37] requires that the integral of the CD spectrum over all wavelengths must vanish, thus we set $m_1 = im_1 e_x$, with $m_1 = 5 \text{ Bohr magneton}$, and $m_2 = im_2 e_y$, with $m_2 = -9 \text{ Bohr magneton}$. The rotational averaging has been achieved by randomly rotating the molecule 150 times, while the Euler angles and rotation matrices have been used. Calculations performed including more rotations showed no significant differences.

A. Results

With the dimer model and mentioned set of parameters, we first calculate the linear absorption and steady-state CD spectra. The calculated results are shown here in Figs. 2(a) and 2(b). In Fig. 2(a), two main peaks are located at 19000 and 21500 cm^{-1} . The calculated CD spectrum is shown in Fig. 2(b), where the main peaks are located at the same frequency values as that of the linear absorption, however, with

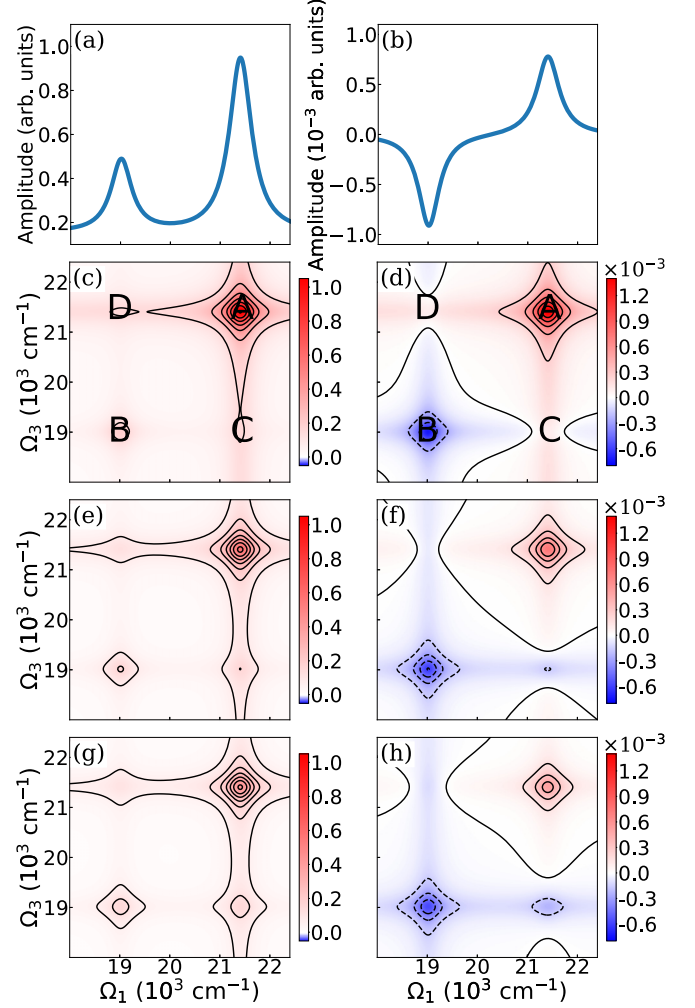


FIG. 2. Transient chiral dynamics of the model molecular dimer. Panels (a) and (b) show the calculated linear absorption and steady-state CD spectra, respectively. The traditional 2DES data (total and real part) of the exciton dynamics at different waiting times are shown as panels (c), (e), and (g). The calculated 2DCD spectra (total and real part) for the same waiting times are presented in panels (d), (f), and (h). The associated excitonic main and cross peaks are marked as A, B and C, D, respectively in panels (c) and (d). The selected waiting times are 0, 2, and 4 ps.

rather weak amplitude. The weaker steady-state CD signals signify that the chiral contribution towards the absorption signal of the dimer is significantly weaker than the achiral contribution.

To analyze the transient chiral dynamics of the energy transfer process in the model dimer, we computed 2DCD spectra (total, real part), which are shown here for selected waiting times in Figs. 2(d), 2(f), and 2(h). The conventional 2DES spectra are also calculated and displayed in Figs. 2(c), 2(e), and 2(g) for comparison. In Fig. 2(c), the 2DES show two diagonal peaks at 19000 and 21500 cm^{-1} , which represent the ground-state bleach, GSB signals (marked A and B). Two cross peaks (marked C and D) demonstrate the existence of excitonic couplings between the two monomers. However, we observe different spectral features in Fig. 2(d) representing 2DCD data: two diagonal peaks marked A and B show the

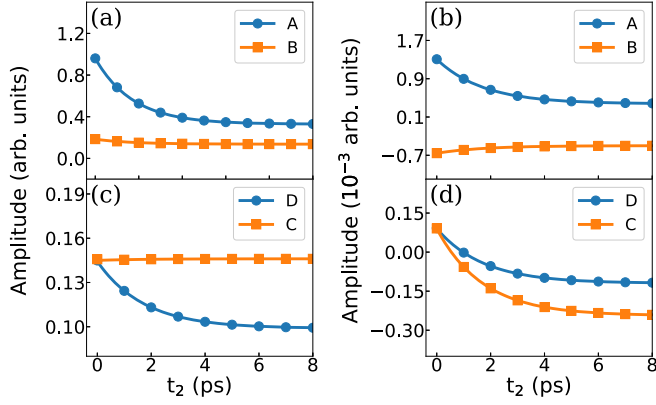


FIG. 3. Time-resolved kinetic traces of the excitonic main (A and B) and cross peaks (C and D), which are marked in Fig. 2. Panels (a) and (c) represent the kinetic traces obtained from the 2DES data, while panels (b) and (d) are kinetics extracted from the calculated 2DCD data.

positive and negative magnitude, which corresponds to the spectral profile of CD spectrum in Fig. 2(b). Two cross peaks (marked C and D) are present but with weak magnitudes, which indicate the weak chiral contribution from excitonic interaction between two monomers. Interestingly, at initial waiting time, the cross peaks C and D show the same spectral profiles. We further calculate the 2DCD spectra evolution with the different waiting times (2 and 4 ps), which are shown in Figs. 2(f) and 2(h), respectively. It shows the magnitude of cross peaks (marked C) increases its absolute value and reach to the maximum at 4 ps. It demonstrates the downhill energy transfer between the two monomers.

To examine the dynamics of energy-transfer process in the model dimer, we also extract the time-resolved traces of the diagonal and cross peaks, shown in Fig. 3. In 2DES data, the diagonal peaks in Fig. 3(a) show the fast decay of magnitude and it reaches to the minimum at 6 ps. The exponential function has been employed to extract the decay constant for the energy-transfer process. The details of fitting and results are shown in the Supplemental Material (SM) [38]. For comparison, we then extract the magnitude of diagonal peaks of 2DCD and plot them in Fig. 3(b) with evolving of waiting time. We also employ exponential function to fit the kinetics and retrieve the decay time constants in the SM [38]. The decay dynamics of cross peaks C and D are shown in Figs. 3(c) and 3(d). In comparison with the 2DES, the 2DCD spectra show the chirality-induced signals and the associated energy transfer in the model dimer system. On the basis of exponential fitting, we obtain that the time constant of population transfer is identical to those retrieved from 2DES (the detailed curve-fitting results and lifetimes are shown in the SM [38]). However, it shows two traces with decay of amplitude in Fig. 3(d) in comparison to the decay and increase in Fig. 3(c). Notably, we do not observe any signature of electronic coherence during the process of energy transfer in Fig. 3, which signifies incoherent nature of the energy-transfer process.

To study transient chiral dynamics of the coherent energy transfer, we perform calculations in strong excitonic coupling regime with different set of parameters: $\epsilon_1 = -50 \text{ cm}^{-1}$, $\epsilon_2 = 50 \text{ cm}^{-1}$, and $J_{1,2} = J_{2,1} = 150 \text{ cm}^{-1}$. The parameters for

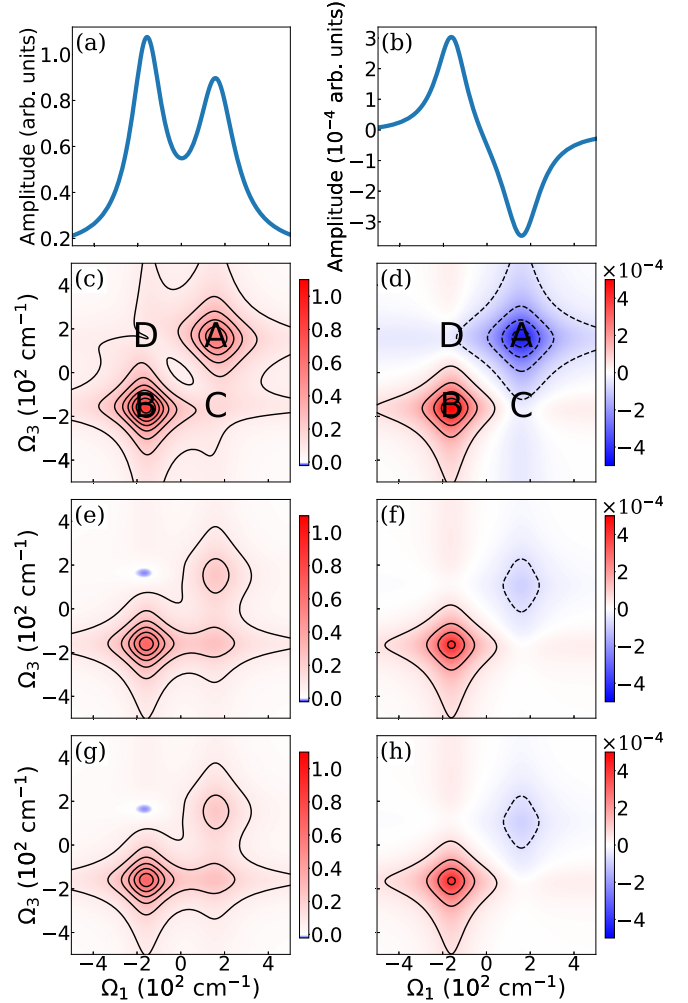


FIG. 4. Transient chiral dynamics of the model molecular dimer under strong excitonic coupling regime. Panels (a) and (b) show the calculated linear absorption and steady-state CD spectra, respectively. The 2DES data of the energy transfer in coupled exciton dynamics at different waiting times are shown as panels (c), (e), and (g). The calculated 2DCD spectra for the same waiting times are presented in panels (d), (f), and (h). The associated excitonic main and cross peaks are marked as A, B and C, D, respectively in panels (c) and (d). The selected waiting times are 0, 400, and 800 fs. Compare with the 2DES, 2DCD presents the magnitude of four orders smaller.

spectral density, $\lambda = 50 \text{ cm}^{-1}$, $\gamma = 150 \text{ cm}^{-1}$, and the environmental temperature is 300 K. Two transition dipoles show $\mu_1 = \mu_1 e_x$, and $\mu_2 = \mu_2 e_y$ with $\mu_1 = \mu_2 = 1$ Debye, $m_1 = im_1 e_x$, and $m_2 = im_2 e_y$, with $m_1 = -m_2 = 1$ Bohr magneton. We calculate the 2DES and 2DCD spectra of the model dimer with strong excitonic coupling and show them in Fig. 4. The calculated linear absorption and steady-state CD spectra are shown in Fig. 4 as Figs. 4(a) and 4(b), respectively. First, we observe two peaks locating at -150 and 150 cm^{-1} . The calculated CD spectrum shows the similar features with positive and negative magnitudes in Fig. 4(b). The time-resolved 2DES and 2DCD spectra are shown in Fig. 4 as Figs. 4(c), 4(e), 4(g) and 4(d), 4(f), 4(h), respectively. For comparison, the main and cross peaks are marked as A, B, C, and D in

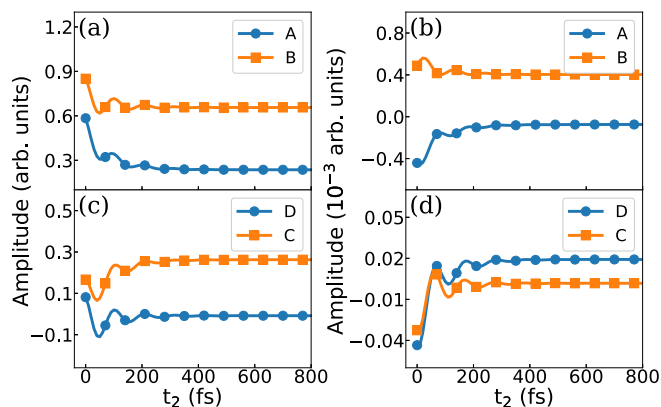


FIG. 5. Time-resolved kinetic traces of the excitonic main (A and B) and cross peaks (C and D) (marked in Fig. 4) in strong excitonic coupling regime. Panels (a) and (c) represent the kinetic traces obtained from the 2DES data, while panels (b) and (d) are the kinetics extracted from the calculated 2DCD data. The orange and blue traces show clear oscillatory dynamics, which is the evidence of electronic coherence. The oscillatory period is 112 fs, which agrees with the energy gap between two electronic states.

Figs. 4(c) and 4(d). In 2DES, two main peaks show positive magnitude, which manifests the GSB signals and the cross peaks demonstrate the excitonic couplings between two monomers. The observed increase of magnitude for peaks B and C signifies the energy-transfer process in the dimer model. However, the time-evolved 2DCD spectra show different kinetics. At $T = 0$ fs, the positive and negative amplitude of diagonal peaks (A and B) indicates the signature of chiral contribution originating from various interactions of electronic- and magnetic-dipole moments. The cross peaks C and D show a rather small magnitude. With the evolution of waiting time, the amplitude of the diagonal peaks decay rapidly at initial 400 fs and then keep a steady value after that. Additionally, the cross peaks do not show any appreciable change of magnitude with time.

To carefully examine the associated energy transfer, we extract the kinetics of diagonal and cross peaks and plot them in Fig. 5. In Figs. 5(a) and 5(c), the time-resolved traces of main peaks show the oscillatory dynamics up to 400 fs, which manifests the electronic quantum coherence induced by the strong excitonic interaction between two monomers. In addition, the evidence of electronic coherence are also present in the kinetic traces of cross peaks in Fig. 5(c). The period of this oscillation is 112 fs, which is in agreement with the energy gap between two excitonic states (300 cm^{-1}). The increase of magnitude of the cross peak [orange line in Fig. 5(c)] manifests the downhill energy transfer from higher excitonic state to the lower one. The decay time constant of energy transfer are obtained by employing exponential fitting, the detailed procedure are presented in the SM [38]. To further retrieve the information on energy transfer in 2DCD, we analyze the kinetics, shown in Figs. 5(b) and 5(d) for diagonal and cross peaks, respectively. In Fig. 5(b), the diagonal peaks indicates the chiral interaction generated after photoexcitation, the fast decay of the magnitude manifests the loss of chiral contribution of interacting monomers in the 2D spectra. The retrieved time constant agrees to those obtained from the

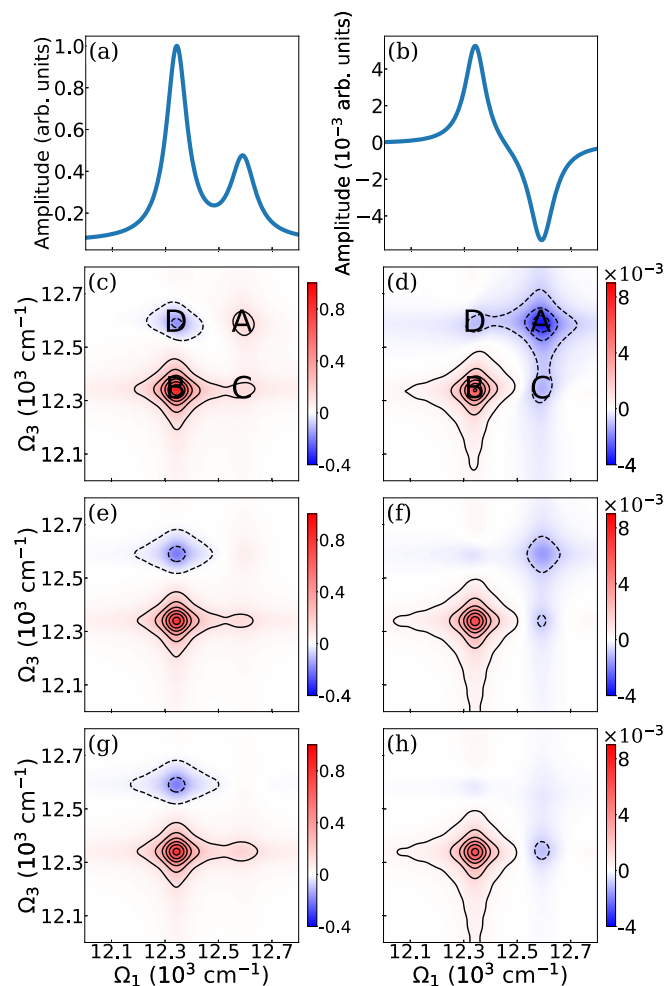


FIG. 6. Transient chiral dynamics of the model molecular dimer of the two pigments from the FMO complex. The absorption and CD spectra are presented in panels (a) and (b). 2DES and 2DCD with selected waiting time of 0, 300, and 800 fs are shown in panels (c), (e), (g) and (d), (f), (h), respectively. The calculated 2DCD data shows clear main and cross peaks for the selected dimer of the natural photosynthetic system.

computed 2DES data. The signatures of electronic quantum coherence is also present in Figs. 5(b) and 5(d). Interestingly, they show opposite phase of oscillations compared with those in Figs. 5(a) and 5(c) of 2DES.

After the calculations and analysis of energy transfer dynamics in molecular dimer in different excitonic coupling regime, we examine the transient chiral dynamics in a natural system to demonstrate its applicability. We select a dimer-system constituting two pigment molecules from the Fenna-Matthew-Olson (FMO) complex. To study the energy transfer and the associated electronic coherence, the dimer system is selected judiciously with relatively strong excitonic coupling with in the pigments (pigment 1 and 2 in Ref. [39]). To study the energy transfer, we perform the calculations and plot 2DES and 2DCD spectra in Fig. 6. The absorption and CD spectra are also shown in Figs. 6(a) and 6(b), respectively. The 2DES and 2DCD with selected waiting time of 0, 300, and 800 fs are shown in Figs. 6(c), 6(e), 6(g) and 6(d), 6(f), 6(h), respectively. In 2DCD [Figs. 6(d), 6(f) and 6(h)], the

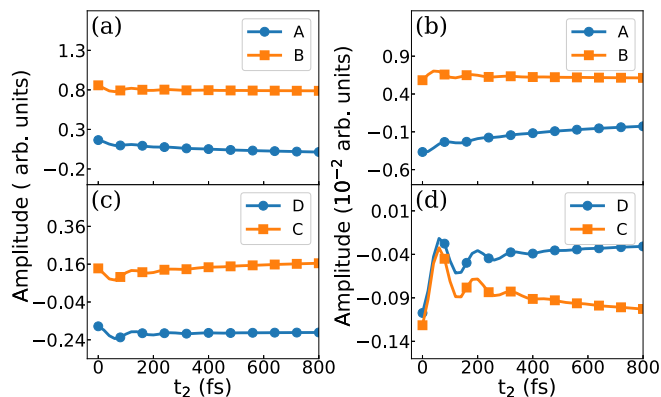


FIG. 7. Time-resolved kinetic traces of the excitonic main (A and B) and cross peaks (C and D) (marked in Fig. 6) obtained from the calculated 2DES and 2DCD are shown in panels (a), (c), and (b), (d), respectively.

cross peak C shows the increase of magnitude (absolute value) with increase of waiting time, which indicates the downhill energy transfer. For all the calculations direction of the dipole moments is conserved as the natural system (i.e., dipoles are not kept parallel or perpendicular to each other). The calculated 2DCD shows featured diagonal and cross peaks similar to above-mentioned special cases of coherent and incoherent energy transfer in different excitonic coupling regime. The respective kinetics are shown in Fig. 7. Importantly, a clear oscillatory dynamics in Fig. 7(d) manifests the electronic quantum coherence during the process of energy transfer. Hence, 2DCD measurements can be very useful to resolve underlying quantum coherences during the energy-transfer process in natural photosynthetic systems.

B. Discussion

We have calculated the 2DCD spectra of a simple dimer model system. We observed that the transient chiral signal of the 2DCD is three order magnitude weaker than the one in 2DES, which makes it challenging for the experimental detection of the signals. We have been motivated to seek an effective approach to enhance the chiral signal, especially, at ultrafast timescale. Recently, plasmon-enhanced chiral dynamics has been performed [40] and the associated steady-state absorption spectrum has been significantly enhanced. Application of plasmonic fields for enhancement

of 2DCD signals may overcome the hurdle in experimental detection of chirality induced transient signatures. Additionally, optical beam with spatial vectors [41] could enhance the absorption spectrum by magnitude of three orders. Hence, the implementation of spatial vectors to measure 2DCD data would provide a powerful optical tool to explore the chiral dynamics in an ultrafast timescale.

Also, a simple dimer model is used in this study. It would be more challenging but at the same time interesting to uncover the chiral population transfer in molecular systems with chiral structure elements such as protein complexes or chiral aggregates. A recent study presented the chiral current circulation and \mathcal{PT} symmetry in a trimer model [42]. On the basis of accurate control of phase of each oscillator, the chiral circulation can be effectively modulated by optical pulses. Hence, we envision that these solutions might pave the way to study the transient chiral dynamics by an ultrafast spectroscopic tool.

IV. CONCLUSIONS

In this paper, we studied the transient chiral dynamics of an excitonically coupled dimer system. We employ the response function theory and made an extension of light-matter interactions with transition magnetic and quadrupole moments to calculate the 2DCD spectra. Based on a simple dimer model, we presented a positive and a negative peak along the diagonal of 2D spectra, which is also the spectral profile associated with the lineshape of steady-state CD spectrum. Moreover, two cross peaks in 2DCD directly manifest the chirality-induced interaction between the two monomers. To study the chiral dynamics in an ultrafast timescale, we calculated the 2DCD spectra for different waiting times and observed the chirality-induced evolution of different spectral features. The downhill energy transfer can be revealed by the dynamics of cross peaks with the associated electronic quantum coherence in strong excitonic coupling regime. We observed that the transient chiral signal is three orders of magnitude smaller than the conventional 2DES signals, which motivates us to enhance the chiral signal by optical or chemical approaches.

ACKNOWLEDGMENTS

This work was supported by NSFC Grant No. 12274247 and the foundation of national excellent young scientist. This work is also supported by Yongjiang talents program. The Next Generation Chemistry theme at the Rosalind Franklin Institute is supported by the EPSRC (V011359/1 (P)).

- [1] E. Pedrueza-Villalmanzo, F. Pineider, and A. Dmitriev, Perspective: Plasmon antennas for nanoscale chiral chemistry, *Nanophotonics* **9**, 481 (2020).
- [2] B. M. Bulheller, A. Rodger, and J. D. Hirst, Circular and linear dichroism of proteins, *Phys. Chem. Chem. Phys.* **9**, 2020 (2007).
- [3] M. Oppermann, B. Bauer, T. Possi, F. Zinna, J. Helbing, J. Lacour, and M. Chergui, Ultrafast broadband circular dichroism in the deep ultraviolet, *Optica* **6**, 56 (2019).

- [4] L. Mangot, G. Taupier, M. Romeo, A. Boeglin, O. Cregut, and K. D. Dorkenoo, Broadband transient dichroism spectroscopy in chiral molecules, *Opt. Lett.* **35**, 381 (2010).
- [5] A. A. Bakulin, S. E. Morgan, T. B. Kehoe, M. W. B. Wilson, A. W. Chin, D. Zigmantas, D. Egorova, and A. Rao, Real-time observation of multiexcitonic states in ultrafast singlet fission using coherent 2D electronic spectroscopy, *Nat. Chem.* **8**, 16 (2016).

- [6] H.-G. Duan, A. Jha, X. Li, V. Tiwari, H. Ye, P. K. Nayak, X. Zhu, Z. Li, T. J. Martinez, M. Thorwart, and R. J. D. Miller, Intermolecular vibrations mediate ultrafast singlet fission, *Sci. Adv.* **6**, eabb0052 (2020).
- [7] F. D. Fuller, J. Pan, A. Gelzinsis, V. Butkus, S. S. Senlik, D. E. Wilcox, C. F. Yocum, L. Valkunas, D. Abramavicius, and J. P. Ogilvie, Vibronic coherence in oxygenic photosynthesis, *Nat. Chem.* **6**, 706 (2014).
- [8] F. Novelli, J. O. Tollerud, D. Prabhakaran, and J. A. Davis, Persistent coherence of quantum superpositions in an optimally doped cuprate revealed by 2D spectroscopy, *Sci. Adv.* **6**, eaaw9932 (2020).
- [9] D. M. Jonas, *Annu. Rev. Phys. Chem.* **54**, 425 (2003).
- [10] H.-G. Duan, V. I. Prokhorenko, R. J. Cogdell, K. Ashraf, A. L. Stevens, M. Thorwart, and R. J. D. Miller, Nature does not rely on long-lived electronic quantum coherence for photosynthetic energy transfer, *Proc. Natl. Acad. Sci. USA* **114**, 8493 (2017).
- [11] E. Thyraug, R. Tempelaar, M. J. P. Alcocer, K. Židek, D. Břina, J. Knoester, T. L. C. Jansen, and D. Zigmantas, Identification and characterization of diverse coherences in the Fenna–Matthews–Olson complex, *Nat. Chem.* **10**, 780 (2018).
- [12] S. J. Jang and B. Mennucci, Delocalized excitons in natural light-harvesting complexes, *Rev. Mod. Phys.* **90**, 035003 (2018).
- [13] D. Abramavicius, B. Palmieri, D. V. Voronine, F. Šanda, and S. Mukamel, Coherent multidimensional optical spectroscopy of excitons in molecular aggregates; quasiparticle versus supermolecule perspectives, *Chem. Rev. (Washington, DC, US)* **109**, 2350 (2009).
- [14] G. Nardin, G. Moody, R. Singh, T. M. Autry, H. Li, F. Morier-Genoud, and S. T. Cundiff, Coherent Excitonic Coupling in an Asymmetric Double InGaAs Quantum Well Arises from Many-Body Effects, *Phys. Rev. Lett.* **112**, 046402 (2014).
- [15] G. Moody, C. K. Dass, K. Hao, C. Chen, L. Li, A. Singh, K. Tran, G. Clark, X. Xu, G. Berghäuser, E. Malic, A. Knorr, and X. Li, Intrinsic homogeneous linewidth and broadening mechanisms of excitons in monolayer transition metal dichalcogenides, *Nat. Commun.* **6**, 8315 (2015).
- [16] L. Bruder, U. Bangert, M. Binz, D. Uhl, R. Vexiau, N. Bouloufa-Maafa, O. Dulieu, and F. Stienkemeier, Coherent multidimensional spectroscopy of dilute gas-phase nanosystems, *Nat. Commun.* **9**, 4823 (2018).
- [17] A. F. Fidler, V. P. Singh, P. D. Long, P. D. Dahlberg, and G. S. Engel, Dynamic localization of electronic excitation in photosynthetic complexes revealed with chiral two-dimensional spectroscopy, *Nat. Commun.* **5**, 3286 (2014).
- [18] M. Cho, Two-dimensional circularly polarized pump–probe spectroscopy, *J. Chem. Phys.* **119**, 7003 (2003).
- [19] J.-H. Choi and M. Cho, Two-dimensional circularly polarized IR photon echo spectroscopy of polypeptides: Four-wave-mixing optical activity measurement, *J. Phys. Chem. A* **111**, 5176 (2007).
- [20] D. Abramavicius, J. Jiang, B. M. Bulheller, J. D. Hirst, and S. Mukamel, Simulation study of chiral two-dimensional ultraviolet spectroscopy of the protein backbone, *J. Am. Chem. Soc.* **132**, 7769 (2010).
- [21] J. R. Rouxel, M. Kowalewski, and S. Mukamel, Photoinduced molecular chirality probed by ultrafast resonant X-ray spectroscopy, *Struct. Dyn.* **4**, 044006 (2017).
- [22] J. R. Rouxel, A. Rajabi, and S. Mukamel, Chiral four-wave mixing signals with circularly polarized x-ray pulses, *J. Chem. Theory Comput.* **16**, 5784 (2020).
- [23] L. P. Chen, R. H. Zheng, Q. Shi, and Y. J. Yan, Two-dimensional electronic spectra from the hierarchical equations of motion method: Application to model dimers, *J. Chem. Phys.* **132**, 024505 (2010).
- [24] L. P. Chen, R. H. Zheng, Q. Shi, and Y. J. Yan, Simulation of the two-dimensional electronic spectra of the Fenna–Matthews–Olson complex using the hierarchical equations of motion method, *J. Chem. Phys.* **134**, 194508 (2011).
- [25] S.-H. Yeh and S. Kais, Simulated two-dimensional electronic spectroscopy of the eight-bacteriochlorophyll FMO complex, *J. Chem. Phys.* **141**, 234105 (2014).
- [26] J. R. Rouxel and S. Mukamel, Molecular chirality and its monitoring by ultrafast X-ray pulse, *Chem. Rev. (Washington, DC, US)* **122**, 16802 (2022).
- [27] E. Rusak, J. Straubel, P. Gladysz, M. Göddel, A. Kedziorski, M. Kühn, F. Weigend, C. Rockstuhl, and K. Slowik, Enhancement of and interference among higher order multipole transitions in molecules near a plasmonic nanoantenna, *Nat. Commun.* **10**, 5775 (2019).
- [28] J. Mun and J. Rho, Importance of higher-order multipole transitions on chiral nearfield interactions, *Nanophotonics* **8**, 941 (2019).
- [29] J.-H. Choi and M. Cho, Quadrupole contribution to the third-order optical activity spectroscopy, *J. Chem. Phys.* **127**, 024507 (2007).
- [30] J.-H. Choi and M. Cho, Nonlinear optical activity measurement spectroscopy of coupled multi-chromophore systems, *Chem. Phys.* **341**, 57 (2007).
- [31] L. Rosenfeld, *Eur. Phys. J. A* **52**, 161 (1929).
- [32] C. R. Cantor and P. R. Schimmel, *Biophysical Chemistry* (W. H. Freeman, San Francisco, 1980).
- [33] W. C. Johnson and I. Tinoco, Circular dichroism of polynucleotides: A simple theory, *Biopolymers* **7**, 727 (1969).
- [34] S. Mukamel, *Principles of Nonlinear Optical Spectroscopy* (Oxford University Press, Oxford, 1995).
- [35] D. Egorova, M. Thoss, W. Domcke, and H. Wang, Modeling of ultrafast electron-transfer processes: Validity of multilevel Redfield theory, *J. Chem. Phys.* **119**, 2761 (2003).
- [36] P. Nalbach, I. Pugliesi, H. Langhals, and M. Thorwart, Noise-Induced Förster Resonant Energy Transfer between Orthogonal Dipoles in Photoexcited Molecules, *Phys. Rev. Lett.* **108**, 218302 (2012).
- [37] E. U. Condon, Theories of optical rotatory power, *Rev. Mod. Phys.* **9**, 432 (1937).
- [38] See Supplemental Material at <http://link.aps.org/supplemental/10.1103/PhysRevE.107.054119> for the Redfield master equation used in the main text, Feynman paths for linear absorption, CD signals and third-order chiral and non-chiral signals, extra results of 2DES and 2DCD at different waiting time, time constants of population transfer.
- [39] H.-G. Duan, A. G. Dijkstra, P. Nalbach, and M. Thorwart, Efficient tool to calculate two-dimensional optical spectra for photoactive molecular complexes, *Phys. Rev. E* **92**, 042708 (2015).
- [40] I. Lieberman, G. Shemer, T. Fried, E. M. Kosower, and G. Markovich, Plasmon-resonance-enhanced absorption and circular dichroism, *Angew. Chem. Int. Ed.* **47**, 4855 (2008).

- [41] L. Ye, L.-Q. Yang, X. Zheng, and S. Mukamel, Enhancing Circular Dichroism Signals with Vector Beams, [Phys. Rev. Lett.](#) **126**, 123001 (2021).
- [42] C. A. Downing, D. Zueco, and L. Martin-Moreno, Chiral current circulation and \mathcal{PT} symmetry in a trimer of oscillators, [ACS Photon.](#) **7**, 3401 (2020).